Heritage Science

RESEARCH

Open Access

Hyperspectral estimation method for deterioration of rock carvings in the humid regions of southern China

Chiwei Chen[1,2], Haiqing Yang[1,2*], Xingyue Li[1,2], Gang Zhao[3] and Jianghua Ni[1,2]

Abstract

Deterioration development is a recognized worldwide threat to rock carvings, especially in humid regions of southern China. Cultural heritage managers thus require precise identification of different deterioration patterns and conduct comprehensive assessments. However, the quantitative analysis of deterioration patterns is limited due to the severe impact of temperature and humidity on rock carvings. Additionally, the current research on the different deterioration patterns is independent, and the corresponding systematic framework is vague. Based on this, the hyperspectral response is constructed to evaluate the various deterioration patterns using spectral index and intelligent model. Firstly, the remarkable correlation between the feldspar content and the deterioration patterns of rock carvings with the influence of environmental factors is investigated by mineralogical analysis. Secondly, combined with microscopic and mineralogical characteristics, the extracted deterioration characteristics are qualitatively screened. Then, a novel spectral index characterizing the correlation between image grayscale and spectral reflectance is proposed by introducing dynamic correction, and the optimal wavelength combination is applied to identify the distribution of deterioration patterns. Consequently, the quantitative screening of deterioration patterns can be realized. After that, the WOA-XGBoost model exhibits better performance in the classification of deterioration patterns. Finally, the influence of different deterioration patterns on rock carvings is quantified by integrating the deterioration index reflected by chemical composition and the proportion of deterioration pattern distribution identified by the spectral response. In the regional deterioration assessment of Dazu Rock Carvings, biological colonization and surface morphological changes have the highest proportion and degree of deterioration, which is worthy of attention in the protection of rock carvings in this region.

Keywords Deterioration patterns, Humid environment, Hyperspectral response, Dazu rock carvings, Intelligent algorithm

Introduction

Rock carvings exposed to the outdoors for a long period of time will inevitably be affected by the rock material, natural environment, and human factors [1–3]. The matrix rock has been damaged by deterioration patterns such as exfoliation, crust, salt crystallization, and biological colonization, even if the majority of rock carvings are well preserved [4–6]. Due to the humid natural conditions in the southwestern region of China, the surface of rock mass is directly impacted by temperature differences, sunlight, wind erosion, and humidity changes [7,

*Correspondence:
Haiqing Yang
yanghaiqing06@163.com; yanghaiqing@cqu.edu.cn
[1] Key Laboratory of New Technology for Construction of Cities in Mountain Area, School of Civil Engineering, Chongqing University, Chongqing 400045, China
[2] National Joint Engineering Research Center of Geohazards Prevention in the Reservoir Areas, Chongqing 400045, China
[3] Academy of Dazu Rock Carvings, Chongqing 402360, China

8]. These factors contribute to the deterioration of the existing more serious. That is why numerous scholars have been concerned in the investigation of deterioration patterns [9, 10]. However, the traditional subjective judgments of visual recognition remain to be used for large-scale areas with multiple deterioration patterns. Thus, it is a current trend to develop an estimation approach that can apply the single deterioration pattern analysis to a variety of deterioration patterns in large-scale areas.

The research on the deterioration patterns of rock carvings is primarily aimed at providing a scientific basis for the protection of cultural heritage. Research on deterioration patterns can be categorized into two main types: one involves the mechanism analysis of deterioration phenomena, while the other focuses on the impact assessment of deterioration patterns.

It is common to evaluate the deterioration degree of rock carvings from the surface phenomenon. However, the description of phenomena alone does not fully elucidate the characteristics of deterioration patterns. Therefore, various investigations are applied for deterioration characteristics analysis. Petrological properties and environmental factors as the primary contributors are discussed in the spatial distribution of various types of deterioration [11]. The humid environment in the rainy season leads to the dynamic change of water saturation on the surface of sandstone, and the subsequent expansion and contraction behavior will promote the development of crust behavior [12]. Meanwhile, water is thought to be a major contributing component frequently involved in various deterioration patterns [13]. Due to the soluble salt composition of groundwater, the long-term accumulation of salt crystals at the boundary of this area is likely to induce rock exfoliation [14]. In addition, there is an intertwined relationship between the weathering and deterioration of the rock mass. Based on the deterioration characteristics, the definition of weathering type can be divided into physical, chemical, and biological [15–17]. Physical weathering can alter the permeability and porosity of rock by affecting its morphology and volume. Furthermore, it provides conditions for further chemical composition change and biological activities. Regrettably, there are numerous evaluation indicators in weathering assessments, but the application corresponding to the specific deterioration model is insufficient. Therefore, it is necessary to investigate the deterioration characteristics by combining the weathering indices with the spatial distribution of various deterioration patterns.

In the formation process of deterioration, affected by external environmental factors, the interaction between particles in the surface layer of the rock mass is gradually weakened, which may result in a loose structure. This changes physico-mechanical parameters and the proportion of mineral components, such as changes in porosity and feldspar content. Consequently, the impact of different deterioration patterns on rock carvings has always been a vague topic in cultural protection.

Since the damage severity of rock is determined by the deterioration pattern, targeted deterioration assessment methods have been proposed in the early stages [18, 19]. Among them, the ability of deteriorated rock mass to resist deformation can be obtained by testing mechanical properties. For example, the protective effect on rocks due to biological deterioration can be observed through surface hardness testing in rock carvings [20]. To further obtain a quantitative description of multiple deterioration patterns, the analysis of mineral and chemical composition is the most intuitive approach [21]. The weathering degree is also defined through the identification of chemical compositions [22, 23]. However, the inversion of deterioration patterns may be impeded by an excess of defined parameters. The hyperspectral technique can be recommended for its sensitivity to the chemical composition of the test sample [24, 25]. It can play a unique role in evaluating the deterioration of rock carvings containing changes in chemical element content. For each deterioration pattern, the hyperspectral data can be regarded as the fingerprint-like dataset, which facilitates the description of characteristic differences. Thus, constructing a spectral database for deterioration patterns based on mineral identification and chemical analysis is meaningful for the deterioration assessment.

This work mainly aims to evaluate the deterioration patterns of rock carvings in humid regions. To develop this approach, the following explorations have been conducted: (i) to determine the mechanism of deterioration patterns on rock carvings in humid environments; (ii) to establish the correlation between hyperspectral data and grayscale value in classification of deterioration patterns; (iii) to apply the optimal spectral index in the deterioration estimation; (iv) to compare the intelligent identification model with optimized parameters in identification of deterioration patterns; and (v) to combine the chemical index in the deterioration assessment of Dazu Rock Carvings induced by various patterns.

Geo-environmental characteristics of research area

Dazu Rock Carvings are selected as a research area because of the complex deterioration patterns. Dazu Rock Carvings are located in the humid regions of southern China, with 105°28′–106°02″ east longitude and 29°23′–29°52″ north latitude. Among them, Baodingshan Grotto is an important representative of Dazu Rock Carvings, which can be considered an outstanding presentation of Chinese grotto art. The landform of

this region is dominated by eroded low mountains in the structure. This region is generally characterized mainly by narrow valleys and deep hillocks, with elevations ranging from 470 to 530 m and terrain elevation differences of about 60 m. As a result, the topographical structure provided a basis for constructing rock carvings and protected them for over 800 years.

The geological map and stratigraphic section of the Baodingshan Grotto are shown in Fig. 1. The overburden of this region is generally loose miscellaneous fill accumulation. Moreover, all exposed strata are sedimentary rocks. In the distribution of bedrock, the upper layer is dominated by fine-grained sandstone within 20 m, and the lower layer is mainly mudstone and sandstone with medium-thick layered interbedded [7]. The strata distribution characteristics with hard over soft have caused the unique landform of cliffs. The prominent canopy structure is formed to protect rock carvings using the strata with better lithology and weathering resistance in the middle layer [26].

Dazu Rock Carvings are characteristics of the cliff statues, which are inevitably exposed to the outdoor environment. Therefore, the external environment plays an essential role in the preservation of rock carvings [27]. The region has a subtropical warm and humid monsoon climate, with an annual average temperature of 17.2 °C. The average annual rainfall is 200 mm more than evaporation due to the influence of the surrounding mountains and atmospheric circulation. Thus, the remaining water become the most important factor causing the deterioration of Dazu Rock Carvings, and various deterioration patterns are aggravated by the participation of water.

The water composition of the Baodingshan Grotto is relatively simple. There is no large surface water in this region, and the groundwater is primarily derived from atmospheric rainfall infiltration. Groundwater can be divided into two kinds according to the location of existence, including the pore water in the overburden and the fissure water in the bedrock fissure. Among them, bedrock fissure water exists in the statue, which is harmful to its preservation. In addition, the majority of the pore water is dispersed across the overburden and flows out through the drainage outlet.

Methodology

Field sampling and analysis

The deterioration of rock carvings in the humid regions of southern China is controlled by the special hydrogeology and microenvironment [21, 28]. Based on these geo-environment characteristics, sampling was carried out at the Baodingshan Grotto of the Dazu Rock Carvings. However, the sampling for the deterioration survey was restricted because of cultural heritage conservation. It is impossible to extract samples directly from the surface of rock carvings. In addition, the deterioration degree of rock carvings varies depending on the structure, position and geology. The response of stratigraphic types of rock carvings to deterioration is different. As a result, the sampling sites require similar environmental and geological characteristics as the rock carvings. Based on the above two factors, the area within 500 m of the main rock carvings and the same stratum as the Jurassic sandstone and mudstone was selected for sampling. Furthermore, the selected sites need to meet the requirements of no rock carvings and obvious deterioration. Considering that the Dazu Rock Carvings have been restored several times in history, the areas selected for sample collection are dominated by the deterioration phenomena of the original rock mass, and rock surfaces with lots of conservation

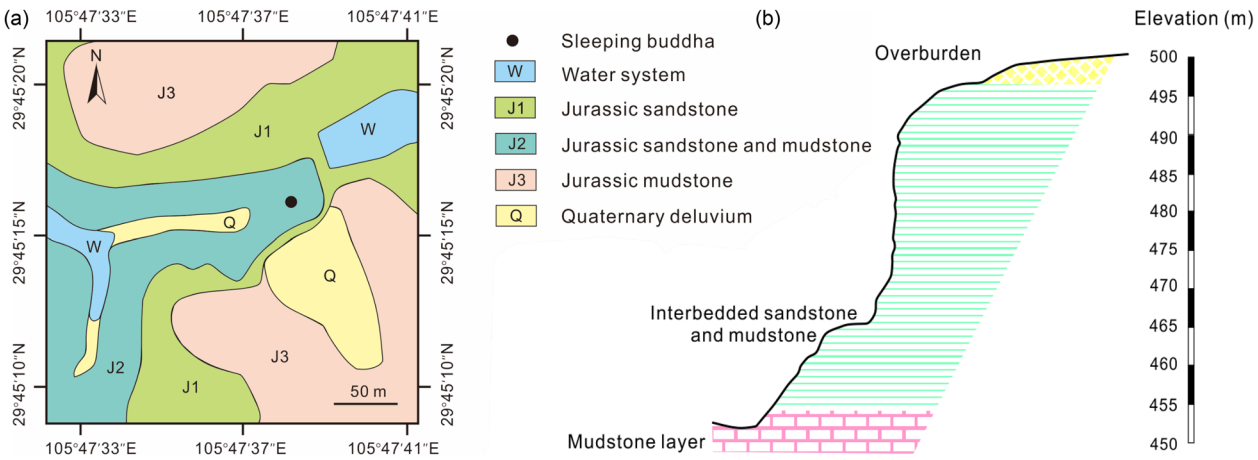

Fig. 1 Geological conditions of Baodingshan Grotto (data from the Academy of Dazu Rock Carvings). **a** Geological map; **b** Stratigraphic profile

materials are avoided as much as possible to ensure the validity of analysis.

The determination of various deterioration characteristics of the Baodingshan Grotto was conducted by testing the collected samples. A total of 50 samples were collected for testing according to the four defined deterioration modes and original state. Then, microscopic petrography, mineralogy, and major elements were used to analyze different deterioration patterns of rock samples [6, 29]. The microstructure of rock samples with different deterioration conditions was observed by the Olympus SZX16 stereomicroscope. Furthermore, the rock thin section identification was measured by the Olympus polarization microscope BH-2. For the mineral composition of rock samples, the powdered rock samples were detected via X-ray diffraction (XRD) using Cu-Kα radiation (Rigaku Ultima IV, Japan; 40 kV; 40 mA; λ = 1.5405 Å). The 2θ angles were set to 10° to 50° and the step size was 0.02°/s during the testing. The chemical composition was analyzed using the alkali fusion method via X-ray fluorescence spectroscopy (ZSX Primus III+, Japan). Moreover, the content of FeO was supplemented by wet chemical analysis. Three repeated tests were performed on the same type of samples to reduce random errors.

Hyperspectral data acquisition and processing

The hyperspectral images were acquired by a portable hyperspectral imaging system in the wavelength range of 400–1000 nm. The system includes a near-infrared spectroscopy (SHIS-N220), a movable tripod, data transmission devices, a 25 cm × 25 cm gray panel with a reflectance of 30%, and a computer supported with the image acquisition software. The effective resolution of the spectroscopy is 2048 × 2046 pixels, and the spectral resolution is 5 nm. This configuration supported the acquisition of millimeter-scale hyperspectral images. In the process of hyperspectral image acquisition, it should be noted that data collection should be selected in an environment with sufficient and stable light. Moreover, the gray panel was used to calibrate the spectral image because the white panel with a reflectance of 99% appeared to be overexposed sometimes. To make the spectral curves comparable, a series of preprocessing steps were performed on the raw spectral reflectance [30, 31]. Each location of the deterioration characteristics was tested five times through the same procedure, and the spectral images were collected in accordance with strict quality assurance and quality control protocols (QA&QC). The specific steps can be summarized as follows.

(i). The reflectance calibration of the raw spectral image was conducted to reduce the noise influence generated by dark current and illumination. The calibration reflectance R_i can be calculated using the following equation:

$$R_i = \frac{R_0 + D_i}{W_i - D_i} \tag{1}$$

where i is the pixel index, R_0 is the reflectance of the raw hyperspectral image, D_i is the reference image of the dark current, and W_i is the reference image of the gray panel.

(ii). The reflectance of the calibrated hyperspectral image was extracted, and the average reflectance of all pixels corresponding to each feature was utilized as the spectral data for subsequent processing.

(iii). The spectral data were processed by normalization, and then reflectance was mapped to the range between 0 and 1. This operation improved the convergence speed of model training, and the influence of data dimension and the difference in value range can be eliminated.

(iv). The normalized spectral reflectance was subjected to the Savitzky-Golay filter to reduce the random noise generated by the device and the environment on the spectral curve. This processing was a smoothing method based on local polynomial least squares fitting. The calculation formula is expressed as:

$$y_j^* = \frac{\sum_{i=-m}^{i=m} w_i y_{j+i}}{N} \tag{2}$$

where y_j^* is the smoothed spectral data, w_i is the weighting of ith value in the smoothing of the moving window, m is the size of the smoothing window, N is the moving window with the value of $2m + 1$.

Image grayscale feature extraction

The deterioration characteristics of rock carvings were taken as the research object. Considering that image acquisition is usually affected by ambient lighting, grayscale processing is required to avoid interference from unstable lighting when acquiring image information [32]. The specific process of the grayscaled image can be divided into three steps: (i) Noise reduction processing of the acquired image. (ii) Followed by extraction of image grayscale features, the grayscale value of the image is within 0 ~ 255. (iii) The spectral reflectance corresponds to the grayscale value in the same region of the image, which is convenient for correlation analysis.

The mean filtering method was used to denoise the image, and the function can be expressed by:

$$P(x,y) = \frac{1}{(2M+1)^2} \sum_{x'=x-M}^{x+M} \sum_{y'=y-M}^{y+M} f(x',y') \tag{3}$$

where $P(x,y)$ is the color feature value of the pixel point at the coordinate (x,y) after filtering; M is the neighborhood radius; $f(x',y')$ is the color feature value of the pixel point at the coordinate (x',y').

The image after noise reduction was grayed by the following:

$$G(x,y) = aR(x,y) + bG(x,y) + aB(x,y) \tag{4}$$

where $G(x,y)$ is the grayscale value of image; a, b, and c are constants, which can be processed by the arithmetic average method, and values can be set as 1/3.

Spectral index selection based on optimal wavelengths

The image can be divided into 160 regions (16×10) before the correlation analysis, and the spectral reflectance and the grayscale response of each region were extracted. Then, the correlation between spectral characteristics and image grayscale response of rock carvings deterioration patterns can be analyzed by spectral indices. Normalized difference index (NDI), difference index (DI), and ratio index (RI) were commonly applied to analyze the correlation through the reflectance of two wavelengths in previous spectral index construction [33, 34]. The calculation of each index is as follows:

$$\mathrm{NDSI} = \frac{R_{\lambda_1} - R_{\lambda_2}}{R_{\lambda_1} + R_{\lambda_2}} \tag{5}$$

$$\mathrm{DSI} = R_{\lambda_1} - R_{\lambda_2} \tag{6}$$

$$\mathrm{RSI} = \frac{R_{\lambda_1}}{R_{\lambda_2}} \tag{7}$$

where R_{λ_1} is the reflectance corresponding to the wavelength of λ_1, R_{λ_2} is the reflectance corresponding to the wavelength of λ_2.

To improve the sensitivity of the characterized object properties, the third wavelength was added to the spectral index calculated in two wavelengths. Referring to the similar forms of three wavelengths [35, 36], new improved spectral indices about three wavelengths were proposed. The whole data set was applied to find the optimal wavelength combination and two correction factors, which can improve the estimation accuracy of the index and enhance the stability of the factor correlation. Thus, the three-wavelength normalized difference index (TNDI), three-wavelength difference index (TDI), and three-wavelength ratio index (TRI) can be expressed as:

$$\mathrm{TNDI} = \frac{R_{\lambda_1} - (R_{\lambda_2} - \alpha R_{\lambda_3})}{R_{\lambda_1} + (R_{\lambda_2} - \beta R_{\lambda_3})} \tag{8}$$

$$\mathrm{TDI} = R_{\lambda_1} - R_{\lambda_2} - \alpha R_{\lambda_3} \tag{9}$$

$$\mathrm{TRI} = \frac{R_{\lambda_1}}{\alpha R_{\lambda_2} R_{\lambda_3}} \tag{10}$$

where α, β are correction factors, which vary from − 3 to 3 (with increments of 0.5), and $R_{\lambda_1} \neq R_{\lambda_2} \neq R_{\lambda_3}$.

Thus, a second screening of deterioration patterns was performed by comparing several spectral indices and selecting the one with the highest correlation coefficient to calculate the response of the hyperspectral image.

Intelligent model for deterioration identification

Based on the superiority of similar studies in feature identification and classification [28, 37, 38], three classification models of eXtreme Gradient Boosting (XGBoost), Random Forest (RF), and Support Vector Machine (SVM) were employed in this study. To further improve the computational efficiency, the built-in parameters of the classification models were optimized using Whale Optimization Algorithm (WOA), Grey Wolf Optimizer (WGO), and Particle Swarm Optimization (PSO) [39–41]. The reasonable parameter settings can improve the accuracy of the classification model effectively. After that, the classification accuracy of various hybrid models was compared.

The classification model for rock carvings deterioration patterns can be developed as follows. (i) A dataset was established with the correlation of spectral reflectance and image grayscale, which consisted of 121 bands of spectral reflectance. (ii) A 7:3 division of the dataset was established between training and testing sets. Among them, training sets were utilized to construct the classification model, while the accuracy of the model in classifying new samples was verified by testing sets. (iii) The objective function was constructed to optimize the built-in parameters of the classification model. (iv) The initialization values were generated by random selection in the parameter range, and the best fitness can be obtained by iterations. (v) The performance of the classification model was evaluated by accuracy after ten training and testing operations.

$$Accuracy = \frac{TP + TN}{TP + FN + FP + TN} \tag{11}$$

where true positive (TP) and true negative (TN) are the numbers of correctly classified positive samples and correctly classified negative samples. False positive (FP) and false negative (FN) are the numbers of misclassified

positive samples and misclassified negative samples. Thus, the flowchart of the hyperspectral estimation method for deterioration of rock carvings in the humid regions of southern China can be illustrated in Fig. 2.

Results

Significant correlation between change of feldspar content and deterioration patterns of rock carvings in humid regions

According to the field investigation of Baodingshan Grotto, the rock carving of the Nine Dragons Bathing the Prince is the main drainage outlet in this area. There are various deterioration patterns induced by the interaction of water and rock. Moreover, the deterioration in this area is more significant than other areas. Thus, the rock carving of the Nine Dragons Bathing the Prince is selected as the object of deterioration patterns analysis, and the distribution map of deterioration is shown in Fig. 3. Combined with the classification of rock carvings deterioration in previous studies [8, 42], the collected typical deterioration characteristics can be presented in Fig. 4. The state of rock carvings can be roughly summarized into five categories, including original state (OS), surface integrity damage (SID), surface morphological change (SMC), surface color change (SCC) and biological colonization (BC). Among them, the influence of rock surface pigments is neglected in the analysis of deterioration. The surface integrity damage is composed of exfoliation and dissolution, and the surface morphology change is mainly caused by the crust phenomenon. Moreover, surface color change is represented by salt crystallization, and biological colonization is manifested as microorganisms and lichens.

Due to the hot and humid environment characteristics in the research area, the rock mass repeatedly undergoes dry–wet alternation, which leads to extensive interlayer pores and loose structures in the microscopic characteristics of different deterioration patterns in Fig. 4. During the collection of typical deterioration phenomena, it is found that exfoliation evolves into fine linear grooves near the bedding plane with the development of deterioration. Moreover, the dissolution and loss of calcareous cement in the rock mass are produced by acid rain, which is a consequence of environmental pollution [43, 44]. Surface morphological change is usually considered to be the result of rock weathering, which may include the combination of allochthonous sediment with original rock. The resulting crust phenomenon shows apparent differentiation of rock thickness and tends to develop into the deep of the rock mass. Affected by the local hot and humid environment, the active fluctuation of temperature and relative humidity leads to the surface color change in the soluble salt crystallization, which is also severe to the rock [45, 46]. In detail, the evaporation effect leads to a continuous concentration of the salt solution from the surface to the interior, which precipitates as crystals on the rock surface. This causes the rock surface to detach or crack. According to field investigation, the edge of the exfoliation is the aggregation position of salt crystals. Furthermore, the deterioration

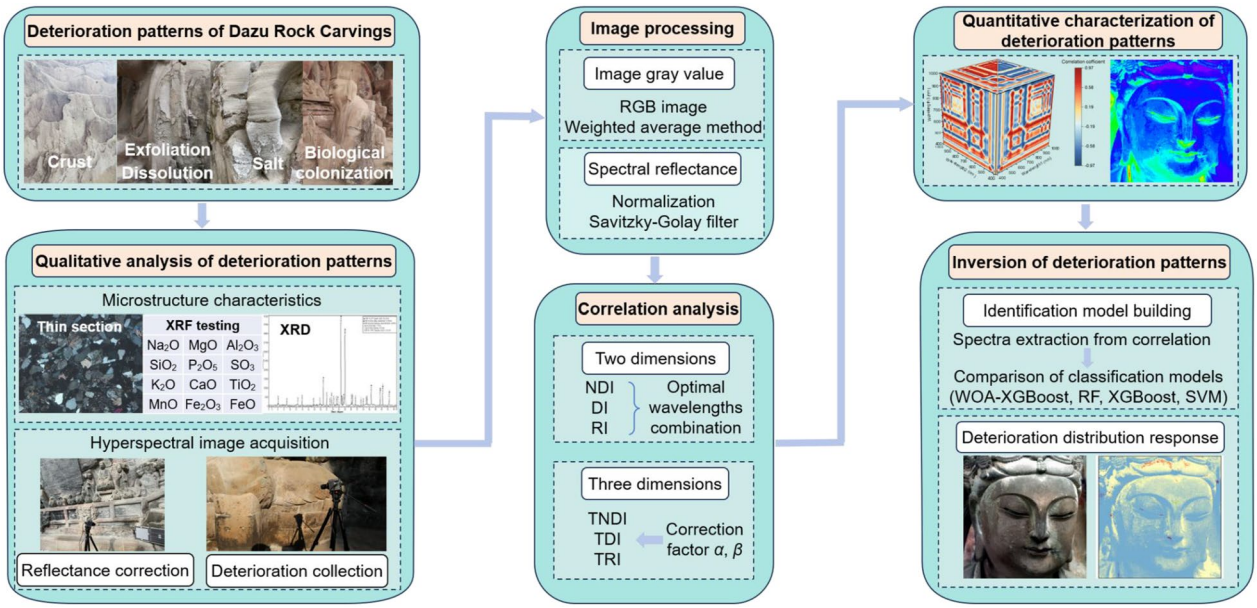

Fig. 2 Flowchart of the hyperspectral estimation method for deterioration of rock carvings

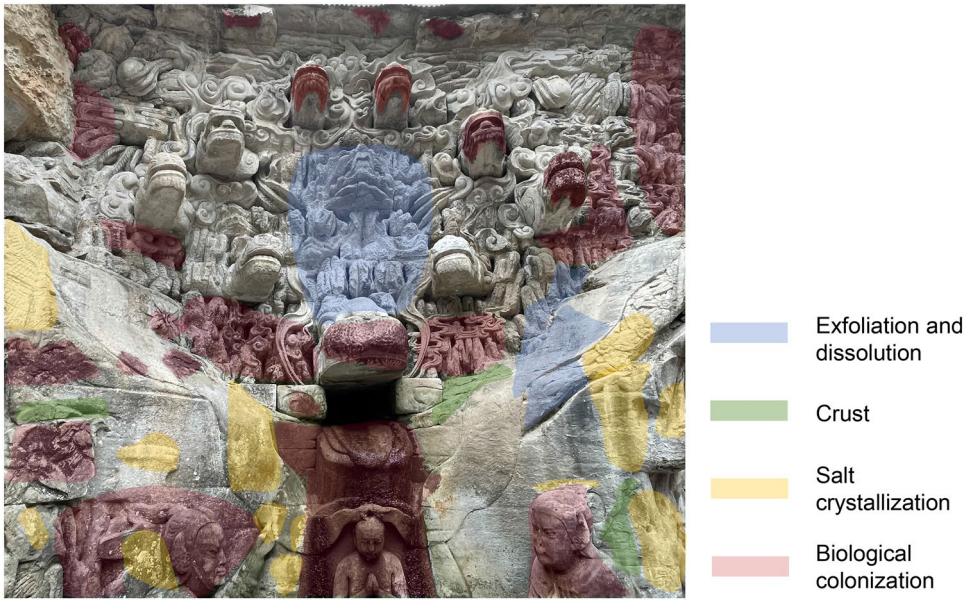

Fig. 3 Deterioration distribution map for rock carving of the Nine Dragons Bathing the Prince

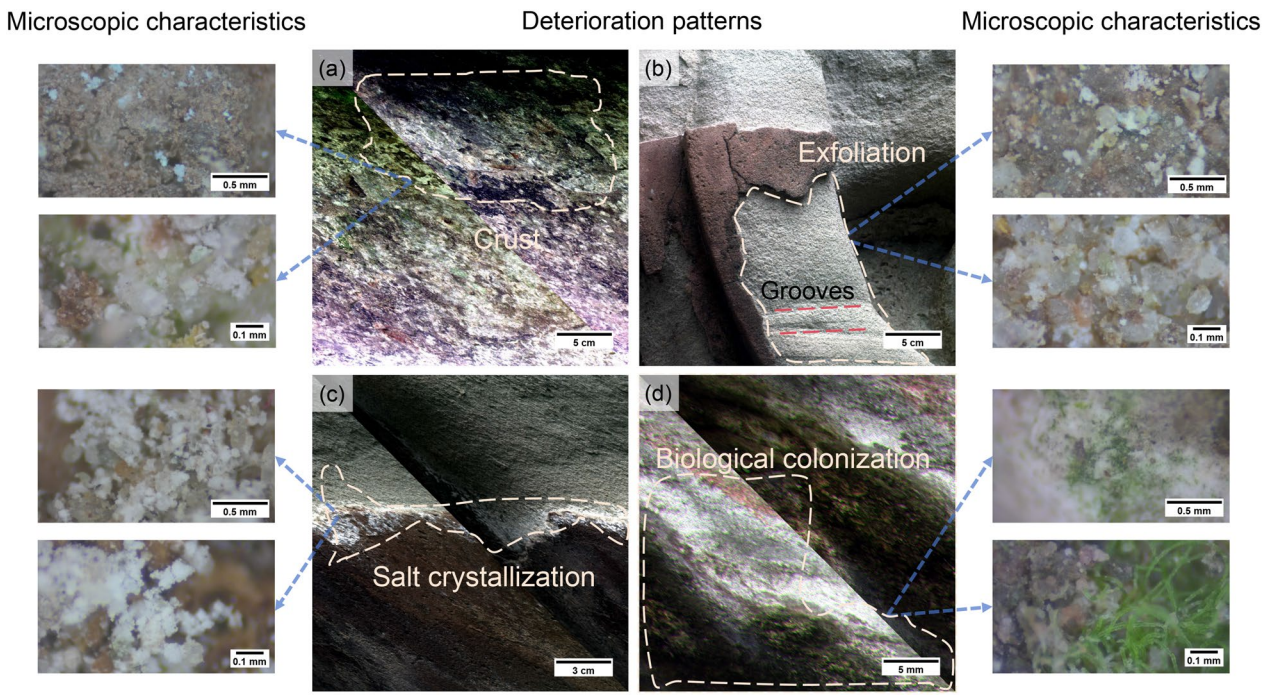

Fig. 4 Typical deterioration phenomena in research area. **a** Roughness changes on rock surface induced by crusts; **b** Exfoliation on the outer surface of rock carvings; **c** Salt crystallization at the edge of exfoliation; **d** Biological colonization of wall surfaces

pattern of biological colonization covers the decoration on the surface of stone statues, and promotes biological erosion of their rock bodies. Moisture provides the basic conditions for biological colonization and affects the rock carvings with biophysical and biochemical effects [5, 47]. For example, moss is frequently accompanied by algae and lichen. The roots develop close to the rock surface or enter the shallow surface of rock along the tiny apertures and constantly secrete acid substances [48]. This action loosens the mineral particles in the shallow layer of the

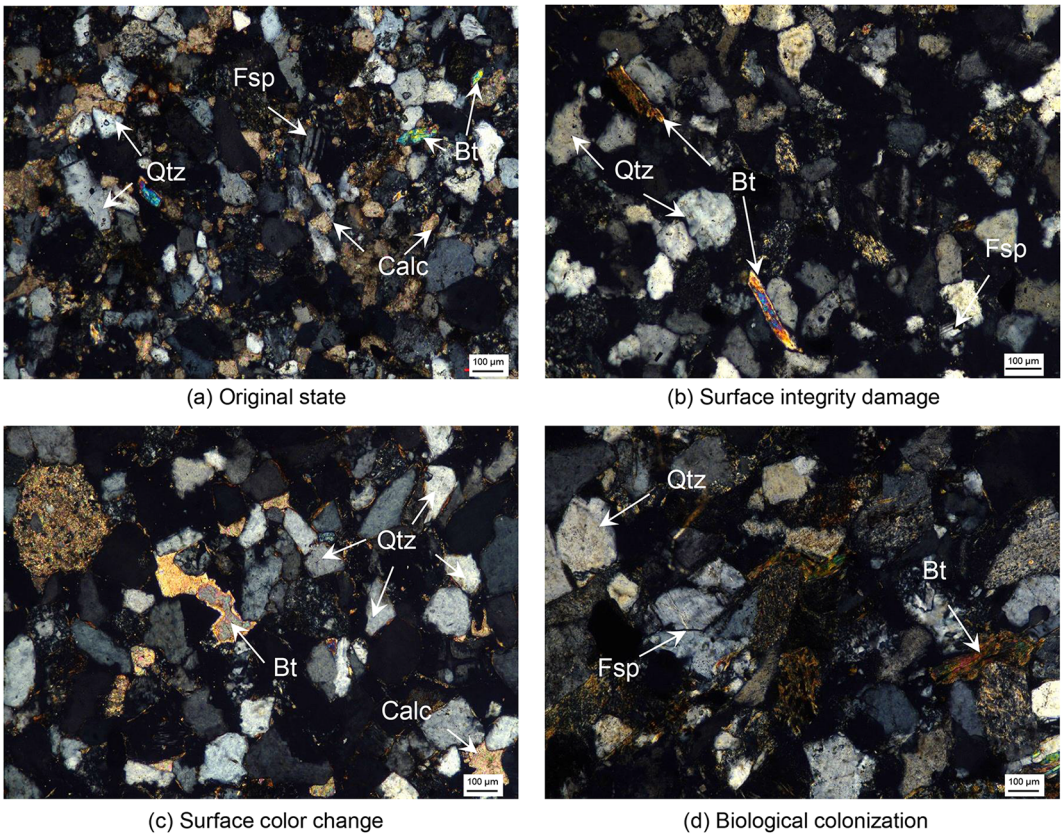

Fig. 5 The characteristics of various patterns in transmitted-light microphotographs. **a** Fine-grained structure presented in the sample with original state; **b** Fine-grained structure presented in the sample with surface integrity damage; **c** Fine-grained sandy structure presented in the sample with surface color change; **d** Fine-grained structure presented in the sample with biological colonization (Qtz: quartz; Fsp: feldspar; Bt: Biotite; Calc: calcium)

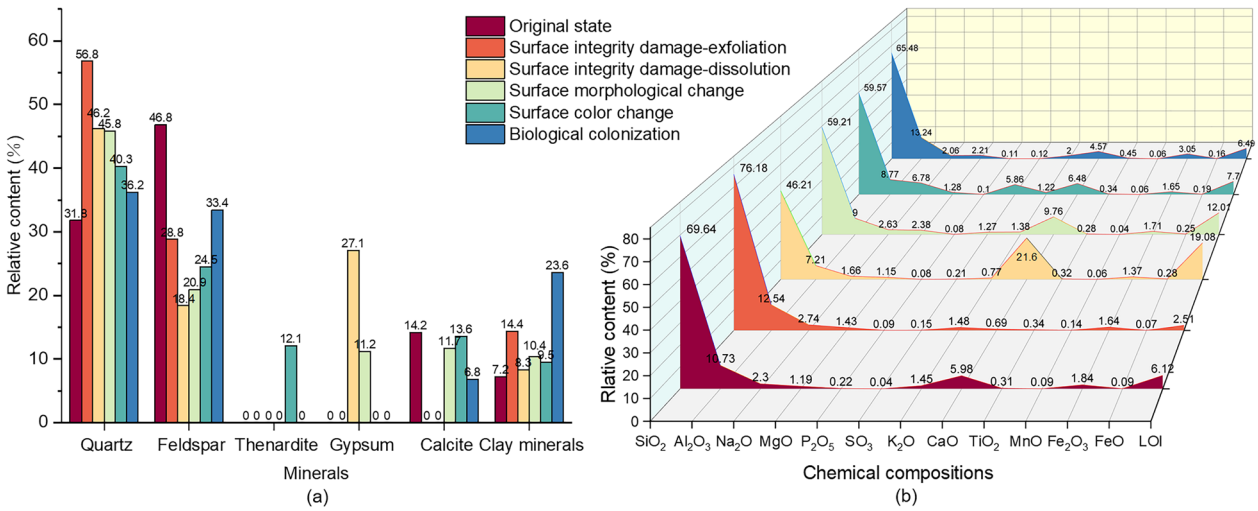

Fig. 6 Identification of samples with different types. **a** Mineralogical composition testing by X-ray diffraction; **b** Chemical composition testing by X-ray fluorescence

rock. It is clear that there are numerous negative aspects in the protection of cultural relics, and all deterioration patterns may overlap and intermingle.

Combined with the identification of the thin section (Fig. 5) and XRD testing (Fig. 6a), it can be seen that the microstructure is presented as fine-grained and sand-shaped with a massive structure. Moreover, they have pore cementation contact. The grain size of the original state is typically in the range of 0.1–0.3 mm, with better sorting. The grain size of SID, SMC, and SCC are concentrated between 0.05 and 0.15 mm, and the grain size of biologically colonized rocks is mostly between 0.15 and 0.2 mm, with the overall grain size of sand showing a tendency to be finer and poor sorting. The mineral composition content of different deterioration patterns can be shown in Fig. 6a.

There is a notable variation in the feldspar content of the mineral composition. Similar studies have found that feldspar dissolution is the most intense feature in humid and acid environments [49, 50]. Compared with the original state, the sandstone samples with the influence of deterioration show a decrease in feldspar content and an increase in the contents of quartz and clay minerals. This indicates that the feldspar is hydrolyzed in the process of sandstone deterioration. The calcite content of exfoliated samples is drastically reduced, which can determine that the exfoliation results in an apparent loss of intergranular calcareous cement. Moreover, the products of feldspar dissolution and clay mineral alteration can be identified as gypsum based on the results of dissolution sample analysis. In the change of surface morphology, the decrease of feldspar and calcite content is replaced by gypsum [51]. It can conclude that the crust layer contains gypsum components. The reason for this deterioration is that acid gas and rainfall in the environment react with sandstone to form gypsum. Meanwhile, the crust is deposited at the junction of dry and wet through rainfall dissolution, and the gypsum surface is blackened due to dust accumulation [52]. The unique mirabilite component of the deterioration behavior of the color change is caused by the salt crystal, which covers the surface of the rock mass. Due to the presence of acid ions in groundwater, the soluble salt crystallizes to the surface as water evaporates when the temperature rises. The sodium sulfate in the soluble salt has obvious deterioration to the rock carvings, and the formation of $Na_2SO_4{\cdot}10H_2O$ during the rainfall process may lead to the expansion of rock mass [27]. In addition, biological colonization also accelerates the dissolution of sandstone, and the proportion of clay minerals increased rapidly from 7.2% to 23.6%, which is the reason for the loose surface. It can be seen from the loss of feldspar that the deterioration of dissolution is the most severe damage to the mineral composition of rock mass. In general, the formation of various deterioration patterns is related to the change of feldspar content, which can serve as a reference index for deterioration analysis.

X-ray fluorescence (XRF) testing is conducted further to analyze the chemical composition of various deterioration patterns. The changes in chemical composition between the exfoliation and the original state are slight. The changes in the decreased contents of CaO, MgO, Fe_2O_3, and FeO, which relate to the characteristic of exfoliation [53]. The main chemical components of feldspar are SiO_2, Al_2O_3, K_2O, Na_2O, and CaO, accounting for more than 80% of the overall content. In contrast, the total amount of soluble oxides (K_2O, Na_2O, CaO, MgO) in the dissolution reaches the highest value of 25.18% among the various deterioration patterns. The percentage of soluble oxides in surface morphological change due to crust is elevated to 16.15% compared to the original state of 10.92%, which suggests that the rock mass is more susceptible to dissolution after crust development. The most significant is that the SO_3 content in surface color change is 146.5 times that of the original state. Therefore, it is determined that the soluble salt crystallization caused by sulfate is the main cause of rock salt weathering in this area. The chemical composition under the influence of biological colonization is higher than the increase of Fe_2O_3 content, and the chemical and biological effects will form iron oxide minerals with a certain degree of crystallinity. Related studies have shown that changes in iron oxide and organic matter are closely related to chemical and biological weathering [54, 55]. Based on the analysis of microscopic characteristics and the correlation of feldspar content, a preliminary screening of deterioration patterns can roughly correspond to the field survey, which can verify the rationality of collected data.

Spectral response for different deterioration patterns of rock carvings

Based on the microscopic characteristics of the initial screening to extract the spectral data of various deterioration patterns, the spectral characteristics are more prominent in the wavelength range of 400–1000 nm after normalization and Savitzky-Golay smoothing in Fig. 7. As shown in Fig. 7b, it belongs to visible light in the range of 400–750 nm and near-infrared light in the range of 750–1000 nm [56]. The subtle differences in deterioration patterns can be characterized by the spectral reflectance in a specific wavelength range. When physical and chemical changes accompany deterioration patterns on the rock, the basic spectral information of the original rock can be retained. In contrast, biological colonization of the rock surfaces is covered by vegetation, which substitutes the spectral information of rock.

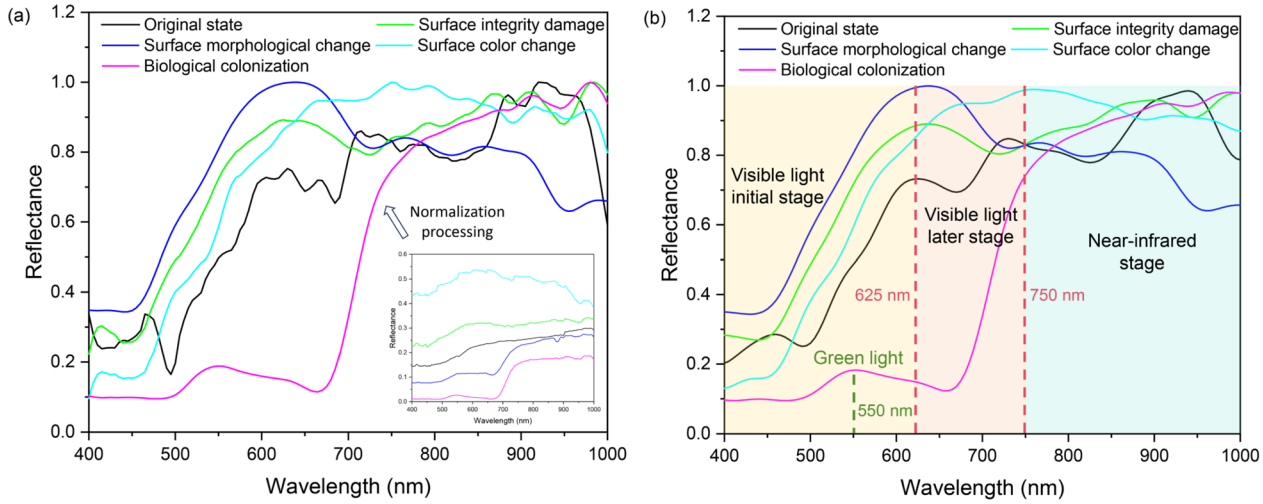

Fig. 7 The average spectral curves of different deterioration patterns in the research area. **a** Spectral curves processed by normalization; **b** Spectral curves filtered by the Savitzky-Golay method

The spectral response presents that different deterioration patterns alter the shape of the spectral reflectance curve. According to the division of visible and near-infrared spectral wavelengths and the shape of spectral curves, it can be roughly divided into three stages: visible light initial stage (400–625 nm), visible light later stage (625–750 nm), and near-infrared stage (750–1000 nm). Among them, the biological colonization is significantly different from the other types of spectral profiles, with a low value of reflectance between 0.09 and 0.18 in the initial stage of visible light. It is worth noting that the absorption peak at the wavelength of 550 nm could be clearly captured in the range of green light, which verifies that biological colonization is affected by the presence of carotenoids and chlorophyll *a* [57, 58]. These factors induce an obvious absorption in the visible light stage, which leads to a low spectral reflectance. After that, spectral reflectance rises rapidly from 0.12 to 0.74 in the late visible light. Existing studies show that the vegetation spectral reflectance curve rises sharply as an almost nearly vertical straight line in the wavelength of visible light [59, 60]. The slope of this wavelength range is closely related to the chlorophyll content per unit area of the vegetation, which are typical spectral characteristics of green plants. The slope of the curve in this range is known as the red-edge phenomenon [61]. The rise slows down in the near-infrared stage and eventually reaches a maximum reflectance.

All four types of spectral curves except for biological colonization show a steep upward trend in the visible light initial stage, and the slopes of the deterioration patterns are larger than those of the original state, and the change of the slopes of the spectral curves may be related to the alteration of the rocks. The relatively strong iron absorption peaks on the spectral curves of deterioration samples result in a significant iron absorption peak near 625 nm [62]. In the visible later and near-infrared stages, fluctuations in the characteristic reflectance are triggered by the absorption peaks of metal cations [45]. In these two stages, the spectral reflectance with surface color changes at the maximum in most cases for all spectral curves. Considering that the surface color change is related to salt crystallization, it is manifested as uniform white powder crystals on the sandstone surface [28]. The presence of salt affects the total brightness of the rock surface, which increases its spectral reflectance. Comparing the spectral curves of the original state and surface integrity damage, the spectral reflectance of the surface integrity damage is greater than the spectral reflectance of the original state in the eighty percent wavelength range. It indicates that the reflectance of the internal fresh rock mass exposed by surface integrity damage will be greater than that of the external undisturbed rock mass. A similar investigation found that the contribution of Fe^{3+} is more outstanding in the external rock mass [63], which is consistent with the XRF testing in Fig. 6b. Furthermore, the roughness of the rock surface and mineral grains might affect the spectral reflectance of the rock. This is reflected in the fact that rocks with relatively high reflectance values have relatively smooth rock surfaces and fine mineral grains [64]. As a result, surface morphology change causes an increase in roughness, which results in lower reflectance values than the original rock in most of the visible later and near-infrared stages. In addition, surface morphology change may produce shadow areas on the rock surface, leading to a lower reflectance of the characteristic absorption peak than

that of the original state. Consequently, the extracted spectral information basically matches each defined deterioration pattern for rock carvings.

Correlation analysis of image grayscale and spectral reflectance

To effectively extract features from hyperspectral images for deterioration identification, optical features are reflected by the grayscale value of images based on the initial screening of deterioration patterns by microscopic features. By coupling the grayscale value and spectral data of pixels, integrated features are applied to distinguish the differences between various deterioration patterns. Based on the spectral data processed by the above spectral preprocessing method, two-dimensional and three-dimensional spectral indices are constructed. Then, the constructed spectral indices can be used to analyze the correlation between spectral reflectance and image grayscale for different deterioration patterns.

The results of the correlation between image grayscale value and spectral reflectance in the spectral indices NDI, DI, and RI are shown in Fig. 8a–c. The x-axis and y-axis denote λ_1 and λ_2, respectively. The deeper colors correspond to a stronger correlation between spectral reflectance and image grayscale value, and the effective region of the correlation can be evaluated by the correlation coefficient in color bars. The response of the three spectral index types varies with the wavelength, and the basic trend is similar. As indicated in Table 1, the optimal wavelength combination with the highest correlation of the spectral index is found at 995 nm and 645 nm, created by the NDI of the preprocessed spectral data.

To improve the correlation of the spectral index, the three-dimensional slice diagrams are applied to further

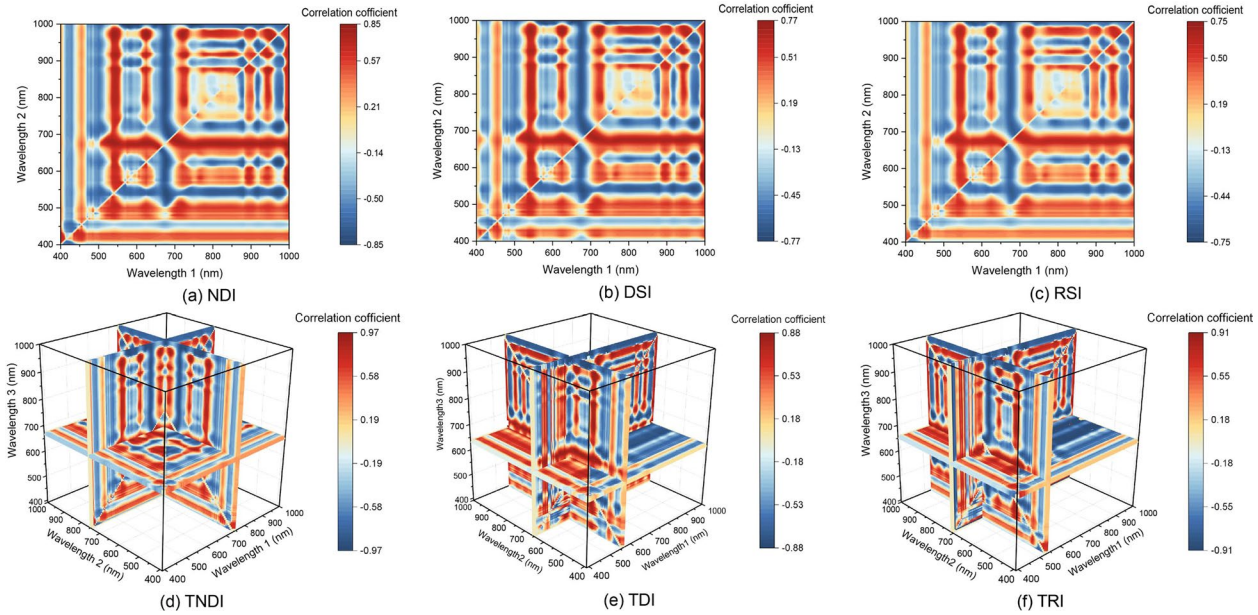

Fig. 8 Correlation diagram of the optimal wavelength combination of image grayscale and spectral reflectance obtained from the spectral indices

Table 1 The optimal wavelength combination of different spectral indices characterizing image grayscale and spectral reflectance

Types	Optimal correction factor	Wavelength 1	Wavelength 2	Wavelength 3	Correlation coefficient
NDSI	–	995	645	–	0.845
DSI	–	995	660	–	0.761
RSI	–	995	645	–	0.742
TNDI	$\alpha=-1, \beta=-1.5$	745	750	670	0.966
TDI	$\alpha=1.5$	565	655	635	0.878
TRI	α = positive number	535	710	655	0.905

explore the potential correlation between spectral reflectance and image grayscale values in Fig. 8d–f. The correlation coefficients of TNDI with different correction factors show the highest correlation in Fig. 9. The x-axis and y-axis denote the correction factors from − 3 to 3 with an interval of 0.5. The TNDI with the two correction factors is more conducive to enhancing the correlation coefficient with the spectral index than the single correction factor. As a result, the correction factors corresponding to the maximum correlation coefficients of three-wavelength spectral indices and the optimal wavelength combinations can be presented in Table 1. The maximum correlation coefficients of TNDI, TDI, and TRI can reach 0.966, 0.878, and 0.905, which is an increase in correlation of 0.121, 0.117, and 0.163 compared to that of NDSI, DSI, and RSI, respectively. Therefore, the sensitivity of the spectral index to the grayscale value of the image can be improved by the addition of a third wavelength [65, 66]. In contrast, the TNDI corresponding to wavelengths 745 nm, 750 nm, and 670 nm by $\alpha = -1$, $\beta = -1.5$ can be identified as the optimal spectral combinations, and the corresponding band calculation formulae are calculated as:

$$\mathrm{TNDI} = \frac{R_{\lambda_1} - \left(R_{\lambda_2} + 1 \times R_{\lambda_3}\right)}{R_{\lambda_1} + \left(R_{\lambda_2} + 1.5 \times R_{\lambda_3}\right)} \tag{12}$$

Hence, the recognition of grayscale for different deterioration patterns can be introduced to extract the accurate spectral data fully, and the corresponding deterioration characteristics are distinguished for the second time.

Discussion

Spectral information for deterioration patterns extracted by optimal wavelength combination

Due to the limitations of the two-wavelength form, the optical information and spectral data of images captured by a two-dimensional spectral index are insufficient. Accordingly, the spectral indices of more than two wavelengths are considered for expansion. The slice diagram obtained from the TNDI has been used to determine the optimal wavelength combination in Fig. 8d, and the corresponding wavelengths 745 nm, 750 nm, and 670 nm of the optimal wavelength combination belong to the visible light range. The increase in the correlation coefficients suggests that the operation of the three-dimensional spectral index contributes to the search for a more sensitive wavelength combination. Studies have shown that the sensitive wavelengths calculated by the optimal spectral index are also related to the characteristic properties of the test substance [36, 67]. The sensitive wavelengths for different deterioration patterns in this study are related to iron elements [45].

Based on the calculation formula of the optimal wavelength combination, the responses of different deterioration patterns in Fig. 4 can be presented in Fig. 10. It

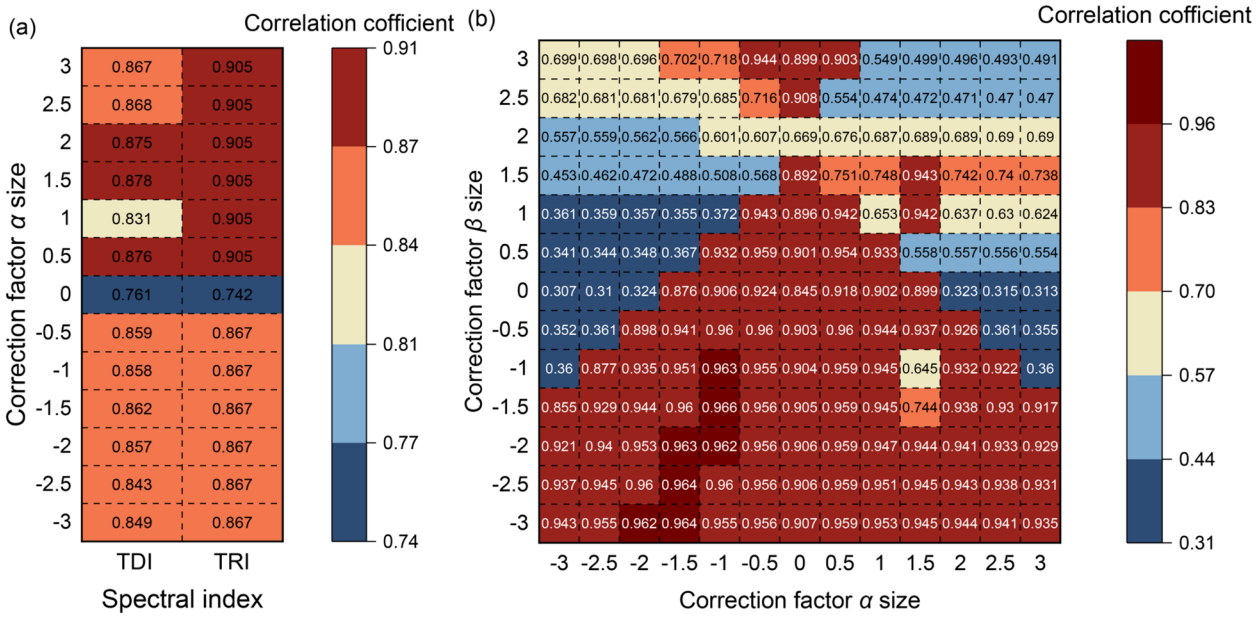

Fig. 9 Correlation coefficients obtained for three-wavelength spectral indices with correction factors. **a** Three-wavelength difference index (TDI) and three-wavelength ratio index (TRI); **b** Three-wavelength normalized difference index (TNDI)

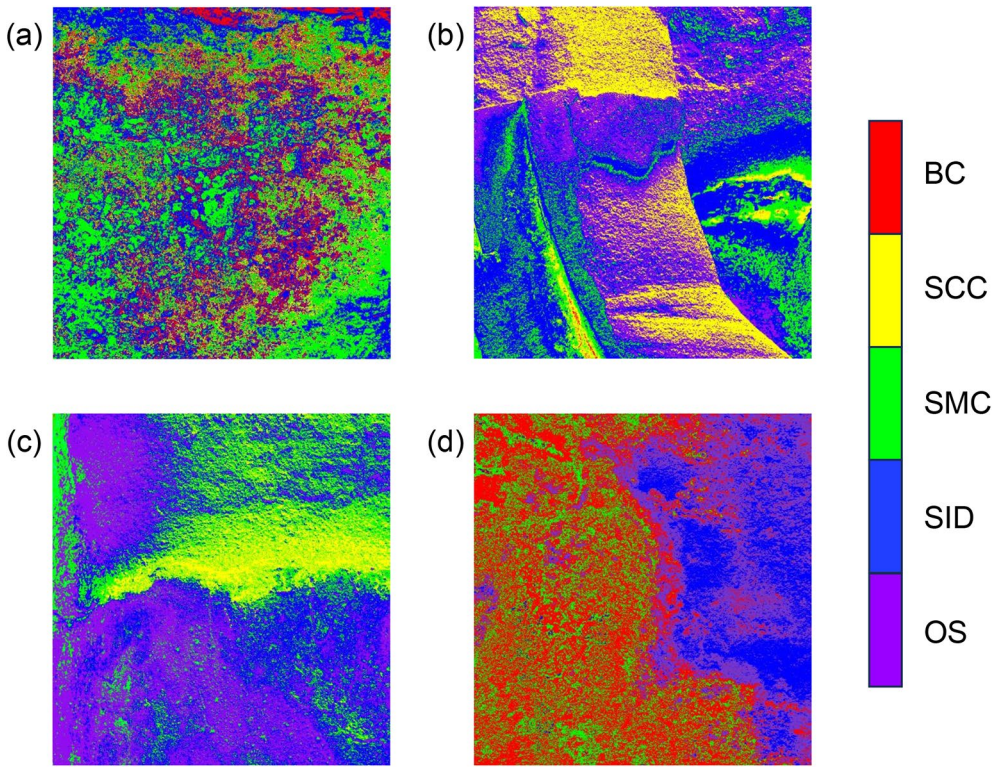

Fig. 10 Response of optimal wavelength combination constructed by the three-wavelength normalized difference index (TNDI) to different deterioration patterns (OS: original state, SID: surface integrity damage, SMC: surface morphological change, SCC: surface color change, BC: biological colonization)

can be seen that the grayscale value and spectral reflectance of each pixel point calculated by the characteristic wavelengths can be sensitive to different deterioration patterns. According to the image processing results of optical influence and spectral reflectance of different deterioration patterns, the distribution of various deterioration characteristics on the rock surface is more accurately displayed than visual observation. The corresponding quantification of each type of deterioration in images can be presented in Table 2, which enables the secondary screening of deterioration patterns.

It can be found in the optical and spectral responses that the defined various deterioration patterns are symbiotic. The most common phenomenon among the various deterioration patterns in humid regions, as illustrated in Fig. 10, is the predominant distribution of surface integrity damage such as exfoliation and dissolution. Exfoliation may cause specific thicknesses of rock fragments on the rock surface to be detached from the rock body. Furthermore, the pores of the dissolved surface are increased, and part of the internal rock is exposed to the air. Water molecules easily infiltrate the bonding interface near the surface of the rock carvings due to the long-term erosion of the humid environment and dissolve with unstable minerals such as feldspar simultaneously [2, 68, 69]. For the results

Table 2 Percentage of optimal wavelength combinations constructed from the three-wavelength normalized difference index (TNDI) in response to different deterioration patterns

Types	Original state	Surface integrity damage	Surface morphological change	Surface color change	Biological colonization
Figure 10a	0	27.91	45.97	9.28	16.84
Figure 10b	27.87	36.88	16.28	18.96	0.01
Figure 10c	37.14	27.05	24.96	10.85	0
Figure 10d	12.83	26.41	19.15	0.05	41.56

calculated by the spectral index, the exposed rock mass after the surface integrity damage in Fig. 10b may cause color brightness and roughness to increase, thus affecting greyscale value and spectral reflectance.

As demonstrated in Fig. 10a, the surface morphology change triggers the rock surface to split and the scattered distribution of small pieces. Meanwhile, there is apparent biological colonization on the crust. The distribution of surface color change can be shown in Fig. 10c, and the precipitated salt particles are comparatively small. In addition to this, the surface color changes caused by salt deposits are concentrated in the cracks, which is similar to the findings of Vázquez et al. [70]. However, the surface color change is often interspersed with surface morphological change, which is generally a coexistence phenomenon. The complexity of the environment further triggers the mutual enhancement between different deterioration patterns [7, 71]. The distribution of the deteriorations in the biological colonization of Fig. 10d seems to be more inclined to develop on the basis of surface integrity damage. The spectral data from the concentrated areas of deterioration patterns in Fig. 10 is extracted separately, thus creating a spectral database for subsequent training of the classification model.

Comparison of classification models in deterioration patterns identification

To classify the hyperspectral data with different deterioration patterns, two tests of the intelligent model are performed. The first test is to compare the results of XGBoost model, RF model, and SVM model for different deterioration patterns, as shown in Fig. 11. The results in the training set show that all types of classification models maintain high accuracy. Thus, it concludes that the reasonableness of the training set can be reflected by extracting from the correlation response of grayscale and spectral reflectance. The second test is for the built-in parameters of the classification model, in which WOA, WGO, and PSO are applied to determine the optimal solutions of the model parameters, as illustrated in Fig. 12. The WOA is superior to other optimization algorithms in searching for the optimal solution of the model parameters so that the preset parameters are replaced by the optimized ones. The combination of XGBoost and WOA is a classification model screened by two feature analysis, which can be used to identify the defined deterioration patterns. The XGBoost model presents an accuracy of 0.912 in distinguishing deterioration patterns. By contrast, the classification accuracy can be improved by 0.039 based on the WOA algorithm. These results show that optimizing the built-in parameters by intelligent algorithms on the training set to obtain the optimal

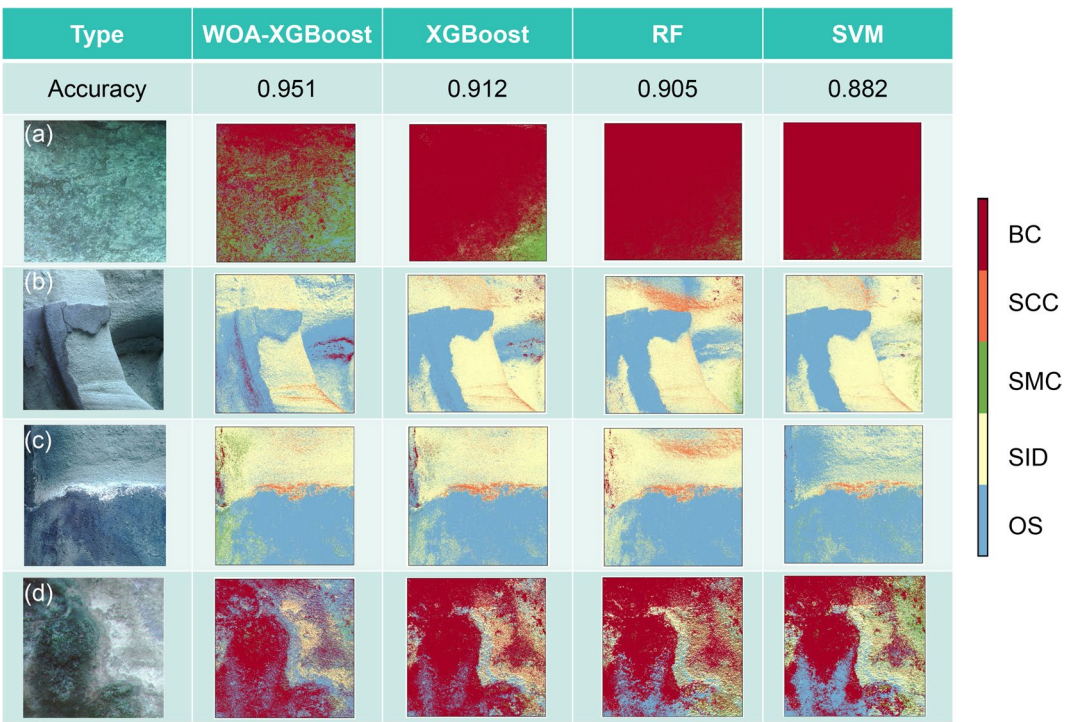

Fig. 11 Inversion of rock carvings deterioration by different classification models. The WOA-XGBoost model shows the highest classification accuracy (OS: original state, SID: surface integrity damage, SMC: surface morphological change, SCC: surface color change, BC: biological colonization)

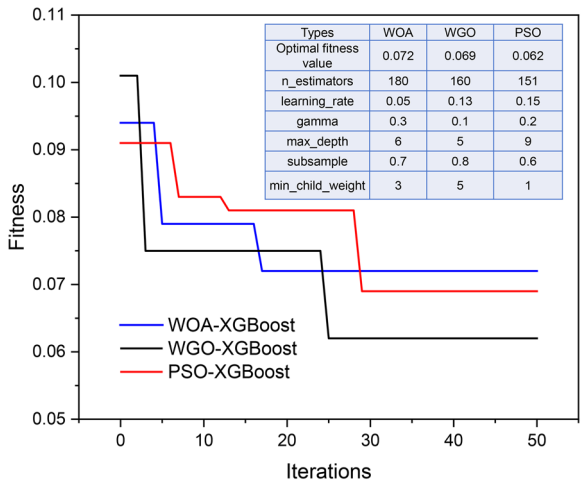

Fig. 12 The built-in parameters of classification model determined by optimization algorithms (XGBoost: eXtreme Gradient Boosting; WOA: Whale Optimization Algorithm; WGO: Grey Wolf Optimizer; PSO: Particle Swarm Optimization)

combination for the deterioration inversion is effective. The optimized classification model identifies each pixel point of the hyperspectral image, which demonstrates the advantages of the method in the classification of deterioration patterns [72–74].

Each pixel point in the image appears to differ in response to deterioration features after recognition by trained models, with each color representing a deterioration pattern. All models provide reasonable and interpretable results that match the visually observed distribution of deterioration patterns. The complexity in the classification of crust and biological colonization can be observed in Fig. 11a. It may produce the largest misclassification areas in this situation, as the presence of significant intersections between these two deterioration patterns leads to only one classification result in most areas. These differences can be explained by the subtle differences in texture and brightness of these two deterioration patterns, which presents a challenge to identify the rock boundaries in images. The WOA-XGBoost model gets the best recognition in distinguishing the crust and biological colonization. It can be seen in Fig. 11b that there are still some limitations in spatial feature recognition. The shaded surfaces may appear under three-dimensional spatial features, which hinders the classification of spectral data in this instance. In the analysis of hyperspectral mineral domain mapping, spatial limitations are also mentioned as major shortcomings in the performance of identification methods [75].

The identification of surface color change in Fig. 11c on the surface of the exfoliated boundary is worth noticing. In detail, the fine-grained features of salt crystallization can be accurately identified in the millimeter-scale hyperspectral images. Figure 11d presents the superposition of multiple deterioration patterns. It is easy to distinguish the deterioration patterns and quantify their spatial distribution, which solves the problem that cannot be differentiated by visual observation effectively. The recognition of WOA-XGBoost maintains steady performance in all case studies, while the other models exhibit some misclassification. These deterioration phenomena confirm the developed classifier as the most robust one. Based on this, the trained model is applied for the field deterioration recognition of rock carvings.

Deterioration assessment of rock carvings characterized by proposed chemical composition change index

The degree of quantifying the deterioration patterns is developed while validating the feasibility of the hyperspectral approach to deterioration identification. As shown in Fig. 13, the optimal model is applied for the rock carving of the Nine Dragons Bathing the Prince to evaluate the effect of spectral recognition. The proportion of deterioration in the selected areas exceeds 50%. Biological colonization is the most common type of deterioration, and surface morphological change accounts for the least proportion. It can be seen from this that although biological colonization makes the surface of rock carvings black, their subtle morphological changes allow the outline of rock carvings to be preserved. The protective or destructive effects of biological behavior on the rock mass have been frequently discussed in previous studies, and related analyses have demonstrated that biological crusts are effective in slowing down the deterioration of the rock mass by physical weathering [76, 77]. Due to the complexity and variability of the environmental conditions in which the rocks are located, there are differences in physical and mechanical properties, mineral composition, and microstructure between weathered rocks and fresh rocks. This difference increases with the degree of weathering. Among them, the significant change in rock chemical composition is considered an essential index for assessing the weathering degree, and existing studies have been conducted to propose a weathering index by comparing the percentage of chemical composition between weathered and original rocks [23, 78]. Referring to related studies, the weathering index (*WI*) can

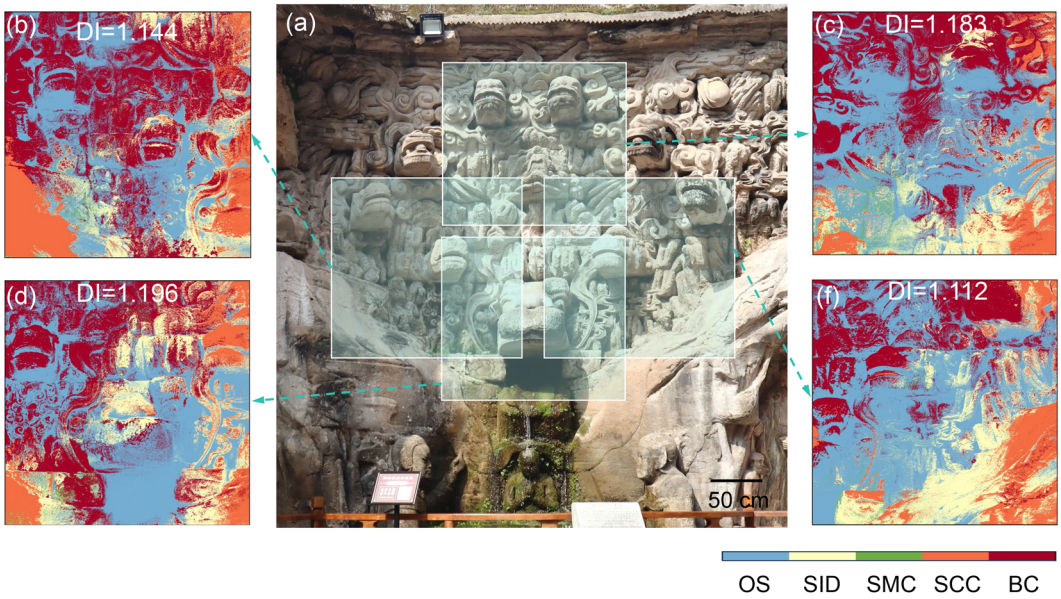

Fig. 13 Quantitative deterioration assessment of the Baodingshan Grotto based on weathering index represented by the chemical composition and the hyperspectral identification of deterioration distribution. There is a positive correlation between the deterioration index (*DI*) and the deterioration degree, which indicates that the middle part of this rock carvings is relatively less deteriorated (OS: original state, SID: surface integrity damage, SMC: surface morphological change, SCC: surface color change, BC: biological colonization)

be expressed as the ratio of weathered rock and original rock:

$$WI = \frac{I_{weathered}}{I_{original\ state}} \tag{13}$$

where I represents a molar ratio of chemical composition. It can be calculated as follows:

$$I = \frac{\left(K_2O + Na_2O + Cao - H_2O^+\right)}{\left(SiO_2 + Al_2O_3 + Fe_2O_3 + TiO_2 + CaO + MgO + Na_2O + K_2O\right)} \tag{14}$$

According to the definition of weathering index, the value is inversely proportional to the weathering degree. Then, the deterioration index (*DI*) can be characterized as the accumulation of various patterns:

Table 3 The comprehensive assessment of different deterioration patterns in Baodingshan Grotto

Deterioration assessment	Original state	Surface integrity damage	Surface morphological change	Surface color change	Biological colonization	Deterioration index
Weathering index	1	0.914	0.528	2.038	0.595	–
Region b	0.323	0.139	0.008	0.199	0.331	1.144
Region c	0.449	0.148	0.017	0.091	0.295	1.183
Region d	0.385	0.176	0.015	0.103	0.321	1.196
Region f	0.441	0.206	0.007	0.125	0.221	1.112

Weathering index is determined by the chemical composition of samples, and the percentage of deterioration patterns in each region is identified by hyperspectral imaging. Deterioration index is calculated by weathering index and hyperspectral imaging, which is proportional to the severity of deterioration

$$DI = \sum \frac{P}{WI} \tag{15}$$

where P is the percentage of deterioration patterns according to hyperspectral image recognition. The value of DI is positively correlated with the deterioration degree. In the deterioration index calculations of this study, the values of the subcomponent in the defined deterioration patterns are averaged.

According to the results of the weathering index of different deterioration patterns in Table 3, the contribution of surface morphological change and biological colonization to the weathering degree is the most significant, while surface color change is the slightest. Similar studies have been conducted that surface morphology change shows notable weathering front along the deep direction of the rock mass in the deterioration evolution, and the weathering index presents a gradual increase from outer to inner layer [22, 70, 79]. Biological weathering is a process of irreversible damage to the rock structure by the physical and chemical effects on the rock matrix by the growth and metabolism of living organisms [47]. Furthermore, when the evaporation effect on the surface of the rock mass is only the salt crystallization phenomenon, which leads to the change of surface color, the weathering degree will be weaker than that of other weathering. The deterioration phenomenon is consistent with the calculated weathering index values obtained for samples taken from humid regions.

Combined with the weathering index and the distribution of deterioration patterns, the deterioration assessment results are shown in Fig. 13. The deterioration values in the middle part of the rock carvings are 1.144 and 1.112 (Fig. 13b and f), which are smaller than 1.183 in the upper part (Fig. 13c) and 1.196 in the lower part (Fig. 13d) of rock carvings. The upper and lower parts of the rock carvings, where biological colonization is concentrated, are found to be the more seriously deteriorated places. Considering that the rock carvings in Fig. 13a contain a diversion tunnel, the water system is developed in this area. Rainfall and surface water migration will both have an impact on the surface of rock carvings. Meanwhile, the wetting front might have a tendency to stay in the middle and upper areas with the capillary action [80]. Significantly less biological colonization occurs in areas with active capillary water. Consequently, it exhibits similar deterioration driven by capillary water migration. Besides, the presence of moisture provides a growth environment for microorganisms and plants surrounding active areas of capillary water. This leads to the destruction of crucial cultural heritage represented on the rock carvings. In general, it is possible to determine the deterioration degree of the rock carvings by correlating the deterioration identification with the weathering degree.

Conclusions

In this study, a method for estimating the deterioration patterns of rock carvings in humid regions of southern China using the hyperspectral imaging technique was established, and its effectiveness was evaluated in Dazu Rock Carvings. The main findings can be presented as follows.

The different deterioration patterns of Baodingshan Grotto under environmental influence can be classified as surface integrity damage, surface morphology change, surface color change, and biological colonization. In the microscopic analysis of various deterioration patterns of rock carvings, the difference in sandstone deterioration can be characterized by mineral proportion and chemical composition, which is regarded as a qualitative identification of deterioration patterns. Specifically, feldspar content and soluble oxides show a strong correlation with deterioration. Also, the grayscale value of images was utilized as an optical indicator to assess the deterioration pattern. According to the grayscale values and spectral reflectance of the images, a three-wavelength spectral index with dual correction coefficients was constructed to identify the corresponding deterioration responses, thus serving as a quantitative identification of the deterioration patterns.

Based on the results of two identification screenings and the preference for intelligent algorithms, the spectral library of various deterioration patterns was applied to the assessment model. The WOA-XGBoost model obtained the best results in the testing of deterioration patterns. In addition, the feasibility of the proposed method was verified for the field deterioration of Baodingshan Grotto by combining the weathering index and the deterioration distribution of spectral identification.

Acknowledgements
We would like to express our appreciation to the Academy of Dazu Rock Carvings for providing essential information on grottos.

Author contributions
HY and CC conceived the study, conducted testing analysis and drafted the manuscript. XL and JN carried out data collection in the study area. CC and XL analyzed the hyperspectral images of deterioration patterns. CC and GZ compared the data with the field phenomenon. HY and CC contributed to the establishment of deterioration models based on spectral and optical data, and critically reviewed the manuscripts. HY and GZ provided financial support. All authors read and approved the final manuscript.

Funding
This research is supported by the Natural Science Fund of China (No. 52179096), the Graduate Research and Innovation Foundation of Chongqing, China (No. CYB23060) and the Natural Science Foundation of Chongqing (No. cstc2021jcyj-msxmX0903).

Availability of data and materials
The data used in this research are published in this paper, and they are all available from the corresponding author upon reasonable request.

Declarations

Competing interests
The authors declare that they have no known completing financial interests or personal relationships that could have appeared to influence the work reported in this paper.

Received: 7 February 2024 Accepted: 23 March 2024
Published online: 29 March 2024

References

1. Jo YH, Lee CH. Weathering features of a five-story stone pagoda compared to its quarrying site in Geumgolsan Mountain, Korea. Environ Earth Sci. 2022;81:181.
2. McAllister D, Warke P, McCabe S. Stone temperature and moisture variability under temperate environmental conditions: implications for sandstone weathering. Geomorphology. 2017;280:137–52.
3. Liu R, Zhang B, Zhang H, Shi M. Deterioration of Yungang Grottoes: diagnosis and research. J Cult Herit. 2011;12:494–9.
4. Martínez-Martínez J, Pola A, García-Sánchez L, Reyes Agustin G, Osorio Ocampo LS, Macías Vázquez JL, Robles-Camacho J. Building stones used in the architectural heritage of Morelia (México): quarries location, rock durability and stone compatibility in the monument. Environ Earth Sci. 2018;77:167.
5. Wu F, Zhang Y, Gu J, He D, Zhang G, Liu X, Guo Q, Cui H, Zhao J, Feng H. Community assembly, potential functions and interactions between fungi and microalgae associated with biodeterioration of sandstone at the Beishiku Temple in Northwest China. Sci Total Environ. 2022;835: 155372.
6. Zhang X, Ling S, Wu X, Xie J. Microscopic weathering mechanisms of subflorescence and crust patterns in the Nankan Grotto, northern Sichuan, China. Herit Sci. 2023;11:181.
7. Zhang J, Li Z, Li L, Liu J, Liu D, Shao M. Study on weathering mechanism of sandstone statues in Southwest China: example from the sandstone of Niche of Sakyamuni Entering Nirvana at Dazu Rock Carvings. Nat Hazards. 2021;108:775–97.
8. Fang H, Zhu S, Ren K. Study on the salt weathering and mechanism of the Banyueshan Giant Buddha in Ziyang City, Sichuan Province, China. Environ Earth Sci. 2023;82:596.
9. Sampietro-Vattuone MM, Peña-Monné JL. Application of 2D/3D models and alteration mapping for detecting deterioration processes in rock art heritage (Cerro Colorado, Argentina): a methodological proposal. J Cult Herit. 2021;51:157–65.
10. Přikryl R, Melounová L, Vařilová Z, Weishauptová Z. Spatial relationships of salt distribution and related physical changes of underlying rocks on naturally weathered sandstone exposures (Bohemian Switzerland National Park, Czech Republic). Environ Geol. 2007;52:409–20.
11. Bruthans J, Filippi M, Schweigstillová J, Rihosek J. Quantitative study of a rapidly weathering overhang developed in an artificially wetted sandstone cliff. Earth Surf Process Landforms. 2017;42:711–23.
12. Siedel H, Pfefferkorn S, von Plehwe-Leisen E, Leisen H. Sandstone weathering in tropical climate: results of low-destructive investigations at the temple of Angkor Wat, Cambodia. Eng Geol. 2010;115:182–92.
13. Alves C, Figueiredo CAM, Sanjurjo-Sánchez J, Hernández AC. Effects of water on natural stone in the built environment-a review. Geosciences. 2021;11:459.
14. Yu S, Oguchi CT. Role of pore size distribution in salt uptake, damage, and predicting salt susceptibility of eight types of Japanese building stones. Eng Geol. 2010;115:226–36.
15. Yang H, Ni J, Chen C, Chen Y. Weathering assessment approach for building sandstone using hyperspectral imaging technique. Herit Sci. 2023;11:70.
16. Huby E, Thomachot-Schneider C, Vazquez P, Fronteau G. Use of micro-climatic monitoring to assess potential stone weathering on a monument: example of the Saint-Remi Basilica (Reims, France). Environ Monit Assess. 2020;192:796.
17. Apollaro C, Perri F, Le Pera E, Fuoco I, Critelli T. Chemical and minero-petrographical changes on granulite rocks affected by weathering processes. Front Earth Sci. 2019;13:247–61.
18. Wu Y, Zhang B, Zhang J, Zhai K, Luo L. Weathering characteristics of white marble relics around the hall of supreme harmony (Taihe Dian) in the Forbidden City. KSCE J Civ Eng. 2023;27:794–804.
19. Lee CH, Jo YH, Kim J. Damage evaluation and conservation treatment of the tenth century Korean rock-carved Buddha statues. Environ Earth Sci. 2011;64:1–14.
20. Wilhelm K, Viles H, Burke O, Mayaud J. Surface hardness as a proxy for weathering behaviour of limestone heritage: a case study on dated headstones on the Isle of Portland, UK. Environ Earth Sci. 2016;75:931.
21. Wang Y, Shao M, Zhang J, Li L, Liang X, Wang N. Quantitative evaluation of alteration and exfoliation in Jurassic sandstone, Chongqing Danzishi rock carvings, China. Eng Geol. 2021;292:106277.
22. Wang K, Xu G, Li S, Ge C. Geo-environmental characteristics of weathering deterioration of red sandstone relics: a case study in Tongtianyan Grottoes, Southern China. Bull Eng Geol Environ. 2018;77:1515–27.
23. Gupta AS, Rao SK. Weathering indices and their applicability for crystalline rocks. Bull Eng Geol Environ. 2001;60:201–21.
24. Petrovic A, Khan SD, Thurmond AK. Integrated hyperspectral remote sensing, geochemical and isotopic studies for understanding hydrocarbon-induced rock alterations. Mar Pet Geol. 2012;35:292–308.
25. Chen C, Yang H, Song K, Liang D, Zhang Y, Ni J. Dissolution feature differences of carbonate rock within hydro-fluctuation belt located in the Three Gorges Reservoir Area. Eng Geol. 2023;327: 107362.
26. Meng Z, Fan F, Cui X, Tao S, Cao Y. Numerical modeling and stability analysis of surrounding rock of Yuanjue Cave. Geofluids. 2021;2021:6652271.
27. Yan S, Xie N, Liu J, Li L, Peng L, Jiang S. Salt weathering of sandstone undera dehydration and moisture absorption cycles: an experimental study on the sandstone from Dazu rock carvings. Earth Surf Process Landforms. 2022;47:977–93.
28. Yang H, Chen C, Ni J, Karekal S. A hyperspectral evaluation approach for quantifying salt-induced weathering of sandstone. Sci Total Environ. 2023;885: 163886.
29. Luo J, Xu Z, Ren Z, Wang K, Gao H, Yang K, Tang Y, Tian L. Quantitative assessment of weathering degree of the Touzhai rock-avalanche deposit in Southwest China. Geomorphology. 2020;359: 107162.
30. Mao Y, Liu J, Cao W, Ding R, Fu Y, Zhao Z. Research on the quantitative inversion model of heavy metals in soda saline land based on visible-near-infrared spectroscopy. Infrared Phys Technol. 2021;112: 103602.
31. Savitzky A, Golay MJE. Smoothing and differentiation of data by simplified least squares procedures. Anal Chem. 1964;36:1627–39.
32. Singh N, Singh TN, Tiwary A, Sarkar KM. Textural identification of basaltic rock mass using image processing and neural network. Comput Geosci. 2010;14:301–10.
33. Tian Y, Zhang J, Yao X, Cao W, Zhu Y. Laboratory assessment of three quantitative methods for estimating the organic matter content of soils in China based on visible/near-infrared reflectance spectra. Geoderma. 2013;202:161–70.
34. Wang X, Zhang F, Ding J, Kung H, Latif A, Johnson V. Estimation of soil salt content (SSC) in the Ebinur Lake Wetland National Nature Reserve (ELWNNR), Northwest China, based on a Bootstrap-BP neural network model and optimal spectral indices. Sci Total Environ. 2018;615:918–30.
35. Zhang Z, Ding J, Wang J, Ge X. Prediction of soil organic matter in northwestern China using fractional-order derivative spectroscopy and modified normalized difference indices. CATENA. 2020;185: 104257.
36. Cao J, Yang H. A dynamic normalized difference index for estimating soil organic matter concentration using visible and near-infrared spectroscopy. Ecol Indic. 2023;147: 110037.
37. Meng X, Bao Y, Liu J, Liu H, Zhang X, Zhang Y, Wang P, Tang H, Kong F. Regional soil organic carbon prediction model based on a discrete wavelet analysis of hyperspectral satellite data. Int J Appl Earth Obs Geoinf. 2020;89: 102111.

38. Samat A, Li EZ, Wang W, Liu SC, Lin C, Abuduwaili J. Meta-XGBoost for hyperspectral image classification using extended MSER-Guided morphological profiles. Remote Sens. 2020;12:1973.
39. Bui QT, Pham MV, Nguyen QH, Nguyen LX, Pham HM. Whale Optimization Algorithm and Adaptive Neuro-Fuzzy Inference System: a hybrid method for feature selection and land pattern classification. Int J Remote Sens. 2019;40:5078–93.
40. Ladi SK, Panda GK, Dash R, Ladi PK, Dhupar R. A novel Grey Wolf Optimisation based CNN classifier for hyperspectral image classification. Multimed Tools Appl. 2022;81:28207–30.
41. Jin X, Song K, Du J, Liu H, Wen Z. Comparison of different satellite bands and vegetation indices for estimation of soil organic matter based on simulated spectral configuration. Agric For Meteorol. 2017;244:57–71.
42. Fitzner B, Heinrichs K. Damage diagnosis at stone monuments -weathering forms, damage categories and damage indices. Acta-Universitatis Carol Geol. 2001;45:12.
43. Eyssautier-Chuine S, Marin B, Thomachot-Schneider C, Fronteau G, Schneider A, Gibeaux S, Vazquez P. Simulation of acid rain weathering effect on natural and artificial carbonate stones. Environ Earth Sci. 2016;75.
44. Gibeaux S, Vazquez P, De Kock T, Cnudde V, Thomachot-Schneider C. Weathering assessment under X-ray tomography of building stones exposed to acid atmospheres at current pollution rate. Constr Build Mater. 2018;168:187–98.
45. Zhao F, Sun Q, Zhang W. Combined effects of salts and wetting-drying cycles on granite weathering. Bull Eng Geol Environ. 2020;79:3707–20.
46. Steiger M, Asmussen S. Crystallization of sodium sulfate phases in porous materials: the phase diagram Na_2SO_4-H_2O and the generation of stress. Geochim Cosmochim Acta. 2008;72:4291–306.
47. de la Rosa JPM, Warke PA, Smith BJ. Lichen-induced biomodification of calcareous surfaces: bioprotection versus biodeterioration. Prog Phys Geogr. 2013;37:325–51.
48. Duane MJ. Coeval biochemical and biophysical weathering processes on Quaternary sandstone terraces south of Rabat (Temara), northwest Morocco. Earth Surf Process Landforms. 2006;31:1115–28.
49. White AF, Bullen TD, Schulz MS, Blum AE, Huntington TG, Peters NE. Differential rates of feldspar weathering in granitic regoliths. Geochim Cosmochim Acta. 2001;65:847–69.
50. Wang C, Chen M, Wang Y. Surface flaking mechanism of stone components of ancient building complex in Wudang Mountain. China Constr Build Mater. 2023;399: 132611.
51. Jin P, Zhang Y, Wang S, Yang X, Zhang M. Characterization of the superficial weathering of bricks on the City Wall of Xi'an. China Constr Build Mater. 2017;149:139–48.
52. Toniolo L, Zerbi CM, Bugini R. Black layers on historical architecture. Environ Sci Pollut Res. 2009;16:218–26.
53. Udagedara DT, Oguchi CT, Gunatilake A. Combination of chemical indices and physical properties in the assessment of weathering grades of sillimanite-garnet gneiss in tropical environment. Bull Eng Geol Environ. 2017;76:145–57.
54. Adamo P, Violante P. Weathering of rocks and neogenesis of minerals associated with lichen activity. Appl Clay Sci. 2000;16:229–56.
55. Patil SM, Kasthurba AK, Patil MV. Characterization and assessment of stone deterioration on Heritage Buildings. Case Stud Constr Mater. 2021;15: e00696.
56. Lim HH, Cheon E, Lee DH, Jeon JS, Lee SR. Classification of granite soils and prediction of soil water content using hyperspectral visible and near-infrared imaging. Sensors. 2020;20:1611.
57. Sims DA, Gamon JA. Estimation of vegetation water content and photosynthetic tissue area from spectral reflectance: a comparison of indices based on liquid water and chlorophyll absorption features. Remote Sens Environ. 2003;84:526–37.
58. Weber B, Olehowski C, Knerr T, Hill J, Deutschewitz K, Wessels DCJ, Eitel B, Büdel B. A new approach for mapping of biological soil crusts in semidesert areas with hyperspectral imagery. Remote Sens Environ. 2008;112:2187–201.
59. Rodríguez-Caballero E, Escribano P, Olehowski C, Chamizo S, Hill J, Cantón Y, Weber B. Transferability of multi- and hyperspectral optical biocrust indices. ISPRS J Photogramm Remote Sens. 2017;126:94–107.
60. Zaady E, Karnieli A, Shachak M. Applying a field spectroscopy technique for assessing successional trends of biological soil crusts in a semi-arid environment. J Arid Environ. 2007;70:463–77.
61. Gitelson AA, Viña A, Ciganda V, Rundquist DC, Arkebauer TJ. Remote estimation of canopy chlorophyll content in crops. Geophys Res Lett. 2005;32:L08403.
62. Stenberg B, Rossel RAV, Mouazen AM, Wetterlind J. Visible and near infrared spectroscopy in soil science. Adv Agron. 2010;107:163–215.
63. Cannon KM, Mustard JF, Salvatore MR. Alteration of immature sedimentary rocks on Earth and Mars: recording aqueous and surface-atmosphere processes. Earth Planet Sci Lett. 2015;417:78–86.
64. Zaini N, van der Meer F, van der Werff H. Effect of grain size and mineral mixing on carbonate absorption features in the SWIR and TIR wavelength regions. Remote Sens. 2012;4:987–1003.
65. Cao Z, Cheng T, Ma X, Tian Y, Zhu Y, Yao X, Chen Q, Liu S, Guo Z, Zhen Q, Li X. A new three-band spectral index for mitigating the saturation in the estimation of leaf area index in wheat. Int J Remote Sens. 2017;38:3865–85.
66. Ryu JH, Oh D, Cho J. Simple method for extracting the seasonal signals of photochemical reflectance index and normalized difference vegetation index measured using a spectral reflectance sensor. J Integr Agric. 2021;20:1969–86.
67. Wang J, Li Z, Jin X, Liang G, Struik P, Gu J, Zhou Y. Phenotyping flag leaf nitrogen content in rice using a three-band spectral index. Comput Electron Agric. 2019;162:475–81.
68. Sato M, Hattanji T. A laboratory experiment on salt weathering by humidity change: salt damage induced by deliquescence and hydration. Prog Earth Planet Sci. 2018;5:84.
69. Ayaz T, Hasan M, Khan A. Petrography and diagenesis of Neoproterozoic Bhander Sandstones, Vindhyan Supergroup, Southeastern Rajasthan, India: implications for provenance and reservoir characteristics. J Sediment Environ. 2023;8:389–407.
70. Vázquez MA, Galán E, Guerrero MA, Ortiz P. Digital image processing of weathered stone caused by efflorescences: a tool for mapping and evaluation of stone decay. Constr Build Mater. 2011;25:1603–11.
71. Waragai T. The effect of rock strength on weathering rates of sandstone used for Angkor temples in Cambodia. Eng Geol. 2016;207:24–35.
72. Othman AA, Gloaguen R. Improving lithological mapping by SVM classification of spectral and morphological features: the discovery of a new chromite body in the Mawat Ophiolite Complex (Kurdistan, NE Iraq). Remote Sens. 2014;6:6867–96.
73. Wang S, Zhou K, Wang J, Zhao J. Identifying and mapping alteration minerals using hySpex airborne hyperspectral data and random forest algorithm. Front Earth Sci. 2022;10: 871529.
74. Thiele ST, Lorenz S, Kirsch M, Acosta ICC, Tusa L, Herrmann E, Möckel R, Gloaguen R. Multi-scale, multi-sensor data integration for automated 3-D geological mapping. Ore Geol Rev. 2021;136: 104252.
75. Lorenz S, Ghamisi P, Kirsch M, Jackisch R, Rasti B, Gloaguen R. Feature extraction for hyperspectral mineral domain mapping: a test of conventional and innovative methods. Remote Sens Environ. 2021;252: 112129.
76. Garcia-Vallès M, Topal T, Vendrell-Saz M. Lichenic growth as a factor in the physical deterioration or protection of Cappadocian monuments. Environ Geol. 2003;43:776–81.
77. Slavík M, Bruthans J, Filippi M, Schweigstillová J, Falteisek L, Řihošek J. Biologically-initiated rock crust on sandstone: mechanical and hydraulic properties and resistance to erosion. Geomorphology. 2017;278:298–313.
78. Topal T. Quantification of weathering depths in slightly weathered tuffs. Environ Geol. 2002;42:632–41.
79. Okewale IA. Applicability of chemical indices to characterize weathering degrees in decomposed volcanic rocks. CATENA. 2020;189: 104475.
80. Huang K, Yu F, Zhang W, Tong K, Guo J, Li S, Chen S, Dai Z. Relationship between capillary water absorption mechanism and pore structure and microfracture of red-layer mudstone in central Sichuan. Bull Eng Geol Environ. 2023;82:100.

Publisher's Note